Materials Science in Additive Manufacturing

ORIGINAL RESEARCH ARTICLE

Gas versus plasma atomized powder in laser powder bed fusion of Grade 5 Ti6Al4V: Processing characteristics and mechanical properties

Jordan Hatch[1], Alex Hicker[1], Chris Liu[1], Alex Montelione[1], Reid Schur[1], Cory Cunningham[2], Mamidala Ramulu[1,2], and Dwayne D. Arola[1,2*]

[1]Department of Materials Science and Engineering, University of Washington, Seattle, WA, United States of America

[2]Department of Mechanical Engineering, University of Washington Seattle, WA, United States of America

***Corresponding author:**
Dwayne D. Arola
(darola@uw.edu)

Citation: Hatch J, Hicker A, Liu C, *et al.* Gas versus plasma atomized powder in laser powder bed fusion of Grade 5 Ti6Al4V: Processing characteristics and mechanical properties. *Mater Sci Add Manuf.* 2026;5(3):026030001.
doi: 10.36922/MSAM026030001

Received: January 15, 2026

Revised: May 14, 2026

Accepted: May 27, 2026

Published online: June 15, 2026

Abstract

Additive manufacturing (AM) of metal components by laser powder bed fusion (L-PBF) has become a viable method of manufacturing in various industries. However, new challenges are emerging, including the high cost of powder feedstock and concerns associated with its reuse. Here, L-PBF was performed with two commercial sources of Grade 5 Ti6Al4V, including commercial plasma-atomized (PA) and gas-atomized (GA) powders. The overall objective was to evaluate differences in the quality, spatial variations in mechanical properties of metal produced with the PA and GA powders over a series of six builds, and to assess if GA powder could be used to replace PA powder for cost savings. The mechanical properties were characterized in uniaxial tension considering powder type, reuse and location within the build envelope. Results showed that the yield and ultimate tensile strength of metal produced with GA powder were significantly lower than that produced with PA powder ($p \leq 0.05$). In addition, spatial variation in the mechanical properties was greatest for the GA powder. The lower strength and greater spatial variation in printing with GA powder appears related to the larger quantity of fines and powder particle satellites, which promote porosity. Overall, the findings indicate that components built with GA powder would: (i) require separate optimization of the printing parameters relative to those used for PA powder, and/or (ii) require additional post-processing to achieve the same performance as those built with PA powder.

Keywords: Laser powder bed fusion; Gas atomized; Plasma atomized; Powder; Porosity; Spatial variations; Strength

1. Introduction

Additive manufacturing (AM) has become a viable approach for near-net- and net-shape manufacturing of components for a variety of industries. While the initial application of 3D printing was focused on rapid prototyping, the vision for AM has evolved substantially, with current focus on the manufacture of complex structures and out of a broad class of materials including ceramics, metals, polymers and composites.[1-5] Metal AM with Ti6Al4V has become of substantial importance due to its potential for achieving desired mechanical properties, corrosion resistance, and high specific strength,[6-9] especially in aerospace.[10-12] However, as the opportunities for industrialization become more realistic,[11] there is an increasing focus on the pain points, which include the cost of the powder feedstock relative to the materials in more traditional manufacturing.

The precise melting of metallic powder during laser exposure of the powder bed enables the use of powder that did not undergo melting to be used in future builds. The reuse of this "unmelted" powder can reduce some of the cost associated with the feedstock for powder bed fusion (PBF) processes. In electron beam melting (EBM) PBF, previous studies have shown that contamination by oxygen can occur with reuse.[1,13-18] However, in L-PBF with Ti6Al4V, Quintana *et al.*[19] showed that recycled powders are oxidized more gradually over sequential builds, with negligible effects on ductility below 0.33 wt%. This evaluation was conducted with plasma-atomized (PA) powder. According to ASTM F2924 for AM with Grade 5 TI6Al4V powder, reuse is acceptable provided that the oxygen content remains below 0.2%. Indeed, numerous investigations have confirmed that powder reuse in L-PBF with Ti6Al4V is highly viable provided that the oxygen remains below that limit.[20-24] One aspect that prevents a clear definition of an accepted or maximum number of reuse cycles is the recycling procedures and whether a replenishment or refresh is practiced. Furthermore, Zhuo *et al.*[21] reported that oxygen uptake was a function of particle morphology, with complex particles sequestering more oxygen relative to smooth particles. That suggests that the local content of oxygen (or other contaminants) could exceed the ASTM limit condition, while the global content remains conforming.

Traditionally speaking, plasma atomization results in very high-quality powders, including spherical particle shape, fewer satellites and with limited impurities.[25-29] Nevertheless, it is an energy-intensive process, which is reflected in the comparatively high cost of powders. The cost factor makes powder recycling necessary to enable L-PBF with Ti6Al4V to be viable. Gas atomization, on the other hand, is a mature technology that has provided feedstocks for the powder metallurgy industry for nearly over a century.[30] Gas-atomized (GA) powder is generally more economical than PA powder. If GA powder feedstock of Ti6Al4V can produce similar quality of metal in L-PBF, then it could serve as a viable option for advancing the industrialization of metal AM.

Properties of the powder feedstock, such as morphology and particle size distribution, are considered important factors that can impact the apparent density, energy absorption and spreadability.[31-35] Yang *et al.*[36] performed an interesting evaluation concerning the importance of powder quality in aluminum alloys using a ray tracing model to simulate energy absorption for various particle size distributions. It was found that the larger particles had higher laser irradiance, decreasing the energy absorbance. As such, confirming the consistency between powder feedstocks is imperative for establishing a baseline property expectation for specific processing parameters. Nandwana *et al.*[37] explored the use of three separate powder feedstocks of Ti6Al4V (produced by plasma-atomized, plasma rotating electrode process, and plasma-wire-atomized powders). They concluded that despite all three powder feedstocks being produced by plasma atomization, there were noticeable differences in the porosity and apparent density. Those differences could be reflected in the printed metal quality and its mechanical properties.

Although prior research has been performed to characterize Ti6Al4V powder for the AM industry, most studies have been focused on the particle and powder characteristics of virgin feedstock and often consider a single powder. Comparatively few studies have performed a holistic evaluation, which involves a comparison of powders and considers reuse and an evaluation of the mechanical properties of the metal produced. Similar research on other alloy systems, including Inconel 718[28] and 304L stainless steel[31] has been fruitful at providing new understanding and helping the industry advance their manufacturing protocols. Due to its high strength to weight ratio and exceptional resistance to corrosion, Ti6Al4V is considered the workhorse alloy of the aerospace industry[38] and is used for a wide variety of stress-critical parts including engine components (*i.e.*, turbine blades, fan discs, *etc.*, as well as landing gear components). Based on its outstanding properties, it is also one of the primary alloys used in the biomedical industry for load-bearing implants.[39] As such, L-PBF of Ti6Al4V has been a research thrust to support the opportunities in these industries.[40-44]

In the pursuit of industrializing L-PBF, powder type, cost and particle characteristics have become recognized as key issues for nearly all alloys.[45-48] That is particularly true in printing with Ti6Al4V.[49-60] Strategies for reducing the cost of printing with Ti6Al4V are needed, but without sacrifices in metal reliability. In this investigation, L-PBF was performed with two different feedstocks of Grade 5 Ti6Al4V, including a GA and a PA powder. The objectives of this investigation were to: (i) characterize the differences in quality and mechanical properties of metal produced with these two different powders, and (ii) assess if GA powder can be used to replace PA powder for cost savings, while achieving the same reliability. Six builds were performed with each powder that consisted of an array of tensile coupons with vertical and horizontal orientations strategically distributed across specific zones of the build chamber. Through a comparison of the mechanical properties resulting from the GA and PA powders of Ti6Al4V, and by quantifying the unique spatial distribution in properties resulting from different powders, the present investigation makes a unprecedented contribution in the expanding literature concerning L-PBF. Results are discussed with respect to differences in the powder characteristics and the properties of the metal produced.

2. Materials and methods

2.1. Materials

Two different powder feedstock materials were used in this investigation. The PA powder was acquired from EOS GmbH and consisted of Grade 5 Ti6Al4V (Product No. 9011-0039; Lot No A 482001) with particle size range from 22 to 61 μm. A comparable GA powder of Grade 5 Ti6Al4V (Ancor Ti; Lot No. 2007910001) was acquired from GKN Ltd with particle size range from 10 to 45 μm. The cost of the GA powder was roughly one-third the cost of the PA powder. The chemical composition of the Ti6Al4V powders described by the Inspection Certificate (IC) and Certificate of Analysis (CoA) that were provided by their manufacturers are shown in Table 1. These values were confirmed by X-Ray Fluorescence Analysis and Inert Gas Fusion.

The builds performed with the PA powder involved clusters of specimens distributed within two levels denoted A and B as shown in Figure 1. On each level the clusters were placed within five zones, indicated as Zone 0 to Zone 4. The clusters in each zone consisted of 10 specimens with vertical orientation, aligned with the z-axis, and 9 specimens in the horizontal plane, aligned with the x axis. Due to limitations posed by the volume of GA powder available, these builds consisted of Level A of the build chamber only (Zones A0 through A4) as shown in Figure 1b. Thus, the builds performed with the two powders were the same, except that only the bottom half of the build chambers was populated in prints performed with the GA powder (*i.e.*, Level A). All the builds were performed using a commercial system (EOS, Model M290, Krailing, Germany) configured with a titanium build plate (EOS DirectBase Ti25, Part No. 220-3440) and a standard HSS recoater blade. The machine uses a 400 W Yb-fiber laser with a focused spot size on the build surface of about 100 μm. High-purity argon (99.998%) was used during the build process to maintain an oxygen-free atmosphere (<0.1%) during the build process.

2.2. Processing

EOSPRINT is an EOS-specific build preparation software used by the EOS M290 for controlling process parameters and exporting the finished file. A standard EOS parameter set for Ti-6Al-4V (Ti64_PerformanceM291 1.10) was used for the builds conducted with both powders used in this study. The critical process variables for the infill are shown in Table 2. It is important to highlight that the default parameters were used for both powders and all builds without further optimization. This choice enabled consistency in processing of the GA and PA powders. Prior work performed by Gordon *et al.*[61] indicates that this is a suitable choice. Two modifications were made to this parameter set to increase the build rate and reduce the total time required to complete the build. First, support structures were melted every other layer, *i.e.*, a layer thickness of 120 μm. Second, contours were turned off for all parts. Scan paths consist of two primary regions: infill and contours. The former, as its name implies, melts the interior of the part. The latter outlines the part, which consequently decreases the surface roughness but increases the residual stresses of the part. Since all coupons were machined before testing, contours were deemed unnecessary and turned off to decrease the laser scanning time and residual stresses.

Six builds were printed with each of the two configurations to characterize property variability, the evolution of properties over multiple builds, and evaluate properties with respect to build location. A schematic diagram outlining the build design and sequence is shown in Figure 1c. Builds 1 and 6 are identical and include specimen clusters populated in each build zone akin to Figure 1a and 1b. To limit powder consumption while maintaining statistical significance, two of the build zones are used in Builds 2 through 5. Note that Zone A0 (at the center) is populated in all builds and provides a source of metal to evaluate properties as a function of incremental reuse. The second build zone populated in each of Builds 2 through 5 (Zones A1 through A4) provides supplemental data that support an evaluation of properties as a function of build location. Over the six builds performed, a total of 342 tensile specimens were printed with the GA powder, including 180 and 162 with vertical and horizontal orientations, respectively. Twice that number of specimens was printed with the PA powder.

2.3. Powder reuse

Powder reuse was performed in this investigation to investigate the relative changes in powder chemistry and

Table 1. Chemical composition of the plasma-atomized (PA) gas-atomized (GA) Ti6Al4V powders

Elements (wt. %)	Al	V	C	Fe	N	H	O	Ti
PA actual [IC]	6.20	4.00	0.01	0.19	0.04	0.004	0.16	Bal.
GA actual [CoA]	6.30	4.10	0.01	0.19	0.01	0.002	0.09	Bal.

Table 2. Key process variables used for the LPBF process

Key process variables	
Laser power	340 W
Hatch rotation	67°
Hatch distance	0.12 mm
Layer height	60 µm
Scan speed	1250 mm/s
Stripe width	5 mm

quality with reuse. The first build conducted with the GA powder was performed with 30 kg. After completion of the build, the powder was extracted from the build chamber and sieved using a 63 µm mesh. Virgin (unused) powder was added to the reused powder with volume consistent with that consumed in the previous build to reach 30 kg for the next build. The powder reuse process is described schematically in Appendix (Figure A1-a**).** The percentage of reused and virgin powder of each build is described in Figure A1-b and the mass composition of each build is listed in Table A1. It is noted that these calculations were constructed under the assumption of perfect mixing to achieve a homogenous distribution and therefore perfect use of aged powder.

2.4. Powder analysis

A small portion of the total powder volume was collected after each build (approximately 150 g), maintained in glass vials, and analyzed using several techniques. Seven samples were collected in total corresponding to powder obtained after the six builds, along with the virgin powder. The samples were dried at 60 °C for 45 minutes under vacuum to remove any moisture and then used for various methods of characterization.

Considering the relatively small particle size of the samples, flowability was analyzed according to the angle of repose, following ASTM C1444-00.[62] Furthermore, the apparent density was measured according to ASTM B212-17 using a conventional density cup.[63] Several taps were applied to aid free flowing through the funnels. In addition, the particle size distribution was tested using a commercial laser scattering particle size analyzer (Horiba Model LA-950, Kyoto Japan).

The particle morphology and size distribution was characterized via scanning electron microscopy (SEM) and optical microscopy (OM). The powder samples were directly sprinkled onto conductive carbon tape for observation. Portions of powder were mounted in resin and then subjected to a sequential polishing process to evaluate the particle microstructure. The polished powder was etched using Kroll's reagent as well.

Light element chemistry was measured for both powders using Inert Gas Fusion (IGF; LECO 836 series elemental analyzer). The IGF assessment provided measurement of oxygen, nitrogen, and hydrogen. The evaluations were performed by Fort Wayne Metals Materials Testing Laboratory (Fort Wayne, Indiana, USA) and were conducted in accordance with ASTM E1409 for oxygen and nitrogen and ASTM E1447 for hydrogen. Each sample was measured three times, with the average chemical values were reported.

2.5. Post-processing

All printed tensile samples were heat-treated to relieve residual stress developed during the build. After the metal was removed from the build plate the heat treatments were performed using a commercial furnace (Nabertherm LH 120/12 f, Bremen, Germany) and under argon environment with the support structures intact. The specimens were arranged to allow for gas circulation during the treatment. The heat treatment program consisted of a one-hour ramp to 745 °C, a two-hour hold at that temperature to anneal, and stress relieve the metal, followed by furnace cooling to room temperature.

Following the heat treatments, the support structures were removed from the builds using an abrasive waterjet (Omax Model 2652, Kent, WA, USA). Thereafter, the tensile specimens were machined to net shape with a Haas TM-1P CNC milling machine using ½” carbide (AlTiN coated) end mills at 500 rpm and with shallow depth of cut (~0.03”) to preserve the microstructure of the specimens and limit potential work hardening. This process was performed to remove surface defects and reduce the surface roughness. The specimens were machined to the dimensions of the sub-sized regular tension specimen as defined by ASTM E8[64] with gauge section dimensions of 6 × 4.5 mm and with a typical roughness of R_a = 0.45 µm, complying with the standard. Only the gage section of the specimens was machined, and the grip sections were left in the as-built condition to aid in gripping.

2.6. X-ray computed microtomography

The metal porosity was evaluated using X-ray computed microtomography (µCT) and was performed using a commercial system (North Star Imaging, Model X5000; Rogers, MN, USA). Scans were acquired on vertically oriented tensile coupons at 100 µA, 100 kV, 1 frame per second and using 2 frame averaging per step, and with 20.83X geometric zoom. A commercial software (VGSTUDIO MAX, Volume Graphics Inc., Charlotte, NC, USA) was used to reconstruct the 1600 projections obtained from each specimen. The scan conditions resulted in approximately 9 µm dimensional resolution of the microstructural features. The porosity was evaluated quantitatively to compute the density of pores within the tensile coupons. In addition, the µCT scans were used to develop quantitative estimates of the pore size and the size distribution, as well as the pore sphericity to distinguish whether the pores were attributed to lack of fusion or gas pores.

2.7. Tensile testing

Tensile testing of the coupons was performed using a commercial system (Instron Model 5585H, Norwood, MA, USA) equipped with a 50 kN load cell and standard wedge grips. The samples were tested in tension to failure under displacement control following the standard ASTM E8 [64] with a crosshead speed of 1.27 mm/mm, which resulted in a strain rate of 0.015 mm/mm/min. The axial strain

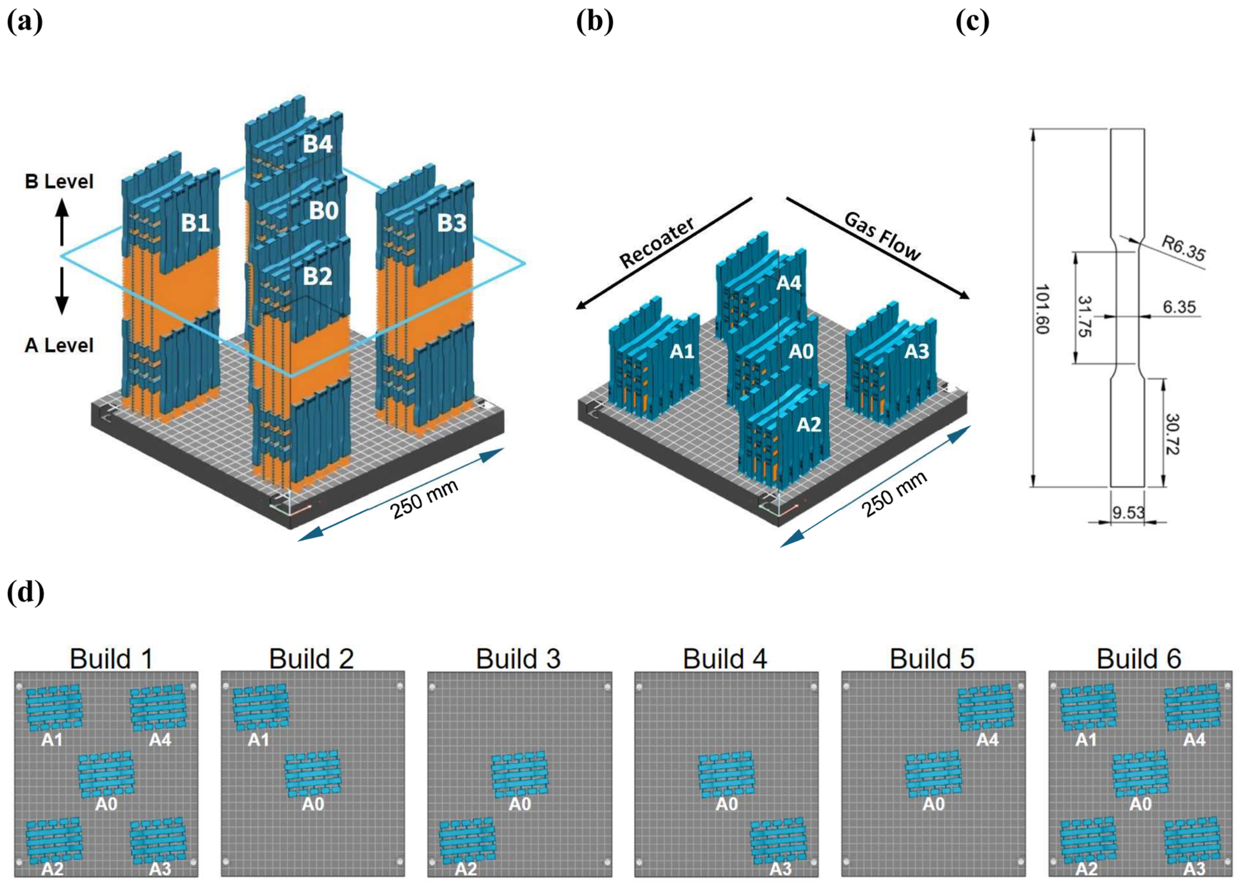

Figure 1. Details of the build design outlining the array of tensile coupons with vertical and horizontal orientations for the builds performed with (a) plasma atomized powders and (b) gas atomized powder. Labels indicate the build zones (0 to 4) on two levels (A and B). Blue indicates dense metal and orange indicates support structure. (c) Dimensions of the tensile specimens in final form (in millimeters). (d) Top view of build designs and occupied zones for the six builds. Note that the builds performed with the PA powder included specimens with the same top view but at two levels (A and B).

was measured using a clip-on extensometer with a 25 mm gauge section. Four samples were tested from each build zone of Level A and with each coupon orientation for the six builds, which resulted in a total of 72 horizontal and 72 vertical coupons for each powder. Overall, a total of 144 tensile tests were performed to failure with the specimens produced from each powder. The remaining specimens were used in complementary activities associated with the investigation.

The force and elongation acquired during the tensile tests were used to determine the mechanical properties of each specimen tested, including the yield strength (YS), ultimate tensile strength (UTS), strain at failure, and tensile toughness. Due to the absence of build metal in the B level with GA powder, the comparison of properties resulting from the two powders was performed for the A level only.

2.8. Fractography

The fracture surfaces of all the tensile coupons were subjected to visual inspections using stereomicroscopy (Olympus SZX16, Evident Scientific, Waltham, MA, USA) to search for the failure origins and further evaluate regions of interest. Thereafter, the fracture surfaces of selected coupons were evaluated by Scanning Electron Microscopy (Apreo-S SEM, ThermoFisher Scientific, Waltham, MA, USA). Most of the fracture surfaces evaluated by SEM were also examined by optical microscopy (Keyence Corporation, Model VR-3000, Itasca IL, USA) to better correlate the features of interest with oblique views of the surface morphology. Some cross-sections were imaged to measure defect size and type between the different print orientations.

Differences in the mechanical properties between the metal produced using PA and GA powder, as well as in terms of the build number were evaluated using a two-way repeated measures analysis of variance (ANOVA). Significant differences were defined for a probability value of $p \leq 0.05$.

3. Results

3.1. Powder

A comparison of the particle morphology of the GA and PA powders is shown in Figure 2. In general, the GA particles exhibit lower sphericity than exhibited by the PA feedstock. In addition, it was noted that the GA powder had more fragmented particles or exhibited larger number of particles with irregular shapes than the PA powder as evident in Figure 3. Open internal gas pores and satellite particles appeared to be more common in the GA powder as well as apparent in Figure 3.

Results from the particle size distribution (PSD) analysis are shown in Figure 4. As evident from this figure, the GA powder has a larger percentage of small particles. Detailed results of the composition measurements including the O, N and H are shown in Table A2 for the first, third, and sixth builds conducted with the GA and PA powders. Results from the IGF analysis showed that the measures of oxygen, nitrogen and hydrogen were far below the limits of the contamination level defined for the Grade 5 Ti6Al4V (ASTM F2924) for both powders.

Additional details of the flow behavior and size distribution measurements for the PA and GA powders are listed in Tables A3 and A4, respectively. These include results from the angle of repose measurements and the apparent density, along with the descriptions for the D10, D50 and D90 size designations. There appears to be a slight decrease in the angle of repose with powder reuse, suggesting that there is an increase in the flowability. However, as noted for the particle size distributions and apparent density, there were no distinct changes in these parameters with powder reuse (Tables A3 and A4). The largest difference in particle size between the two powders is reflected in the D10 measures.

3.2. X-ray computed microtomography

Results obtained from x-ray computed microtomography and complementary analysis of the porosity of the tensile specimens are shown in Figure 5. This figure describes the overall pore distribution for the powder feedstocks in terms of the effective diameter and the pore sphericity. As evident from this figure, the effective pore diameter ranges from roughly 30 to over 300 μm. There are no distinct differences in the pore diameter distribution between the metal produced with GA and PA powders. However, as evident in Figure 5, the metal printed with GA powder exhibits a larger number of pores with diameter ≥ 100 μm. There are also size effects that could be relevant here, increasing the potential degradation of metal properties with increase in pore diameter. Between the two powders, the distribution of pores in the tensile coupons built with GA powder is shifted to the left, indicating an overall lower sphericity of pores in comparison to the PA metal. The pore classification was primarily performed through the size and aspect ratio (*i.e.*, sphericity) as evident from Figure 4. The sphericity and size reflect that most of the pores identified have effective diameter that is equal to or greater than the powder particles. As such, these are unlikely to be pores originating from within powder particles. Gas pores are possible, but the aspect ratio shows that they are not prominent. Lastly, keyholes would be evident from their orientation perpendicular to the layers, which were not evident. Most voids were of the lack of fusion (LOF) type for both powders.

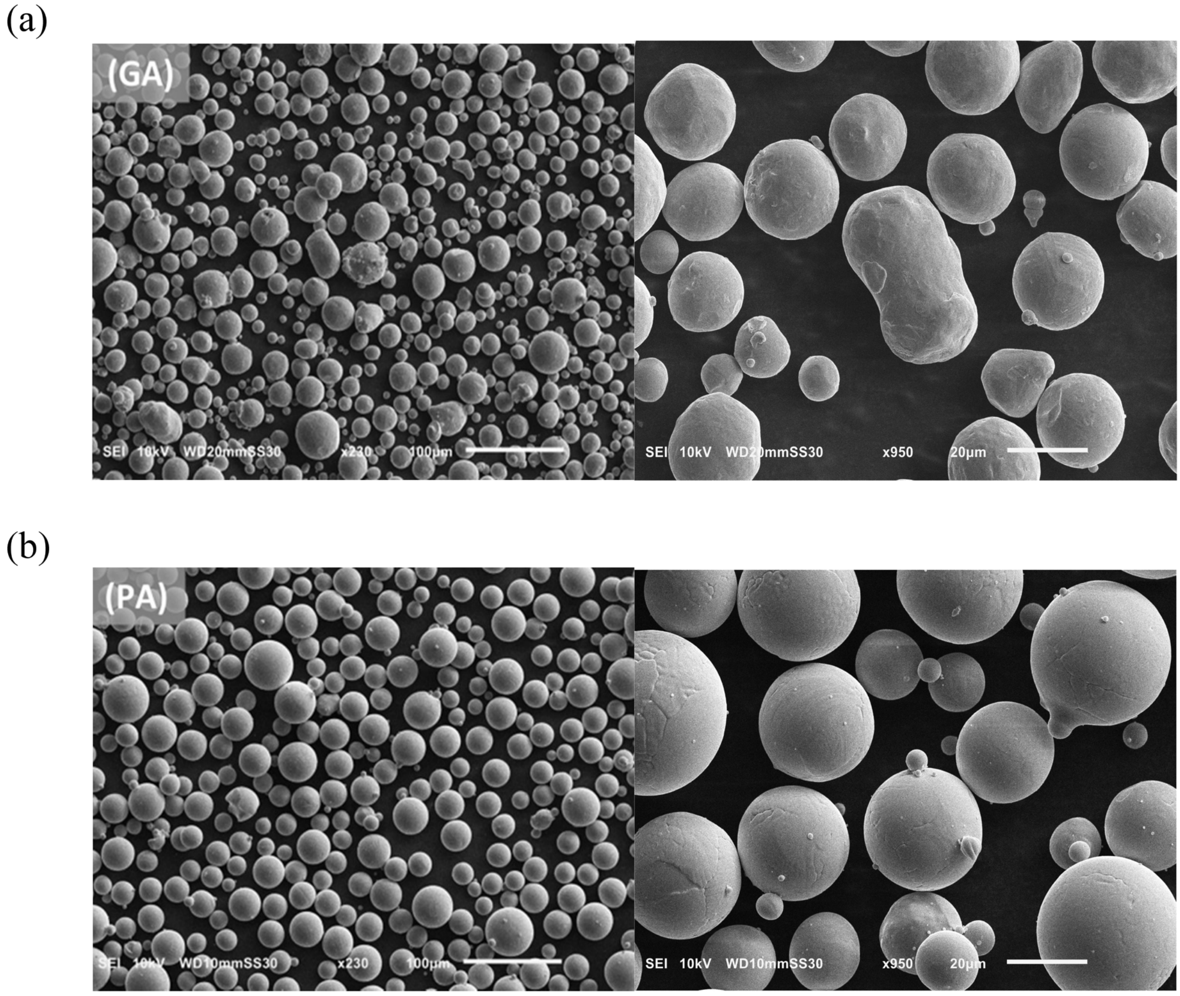

Figure 2. Representative scanning electron microscopy (SEM) images of the particle morphologies of the (a) virgin GA and (b) PA Ti6Al4V powder prior to printing.
Abbreviations: GA: Gas-atomized; PA: Plasma-atomized.

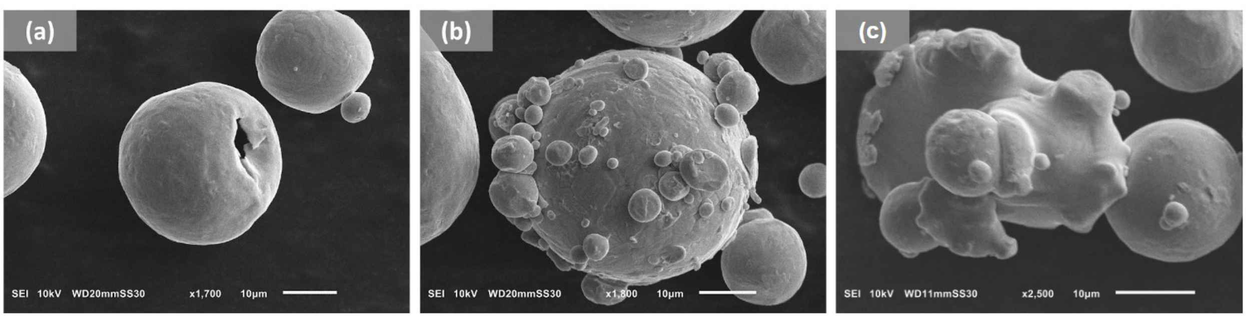

Figure 3. Representative images of defect characteristics observed in the virgin gas-atomized (GA) powder, including (a) internal pores, (b) satellite particles, and (c) spatter

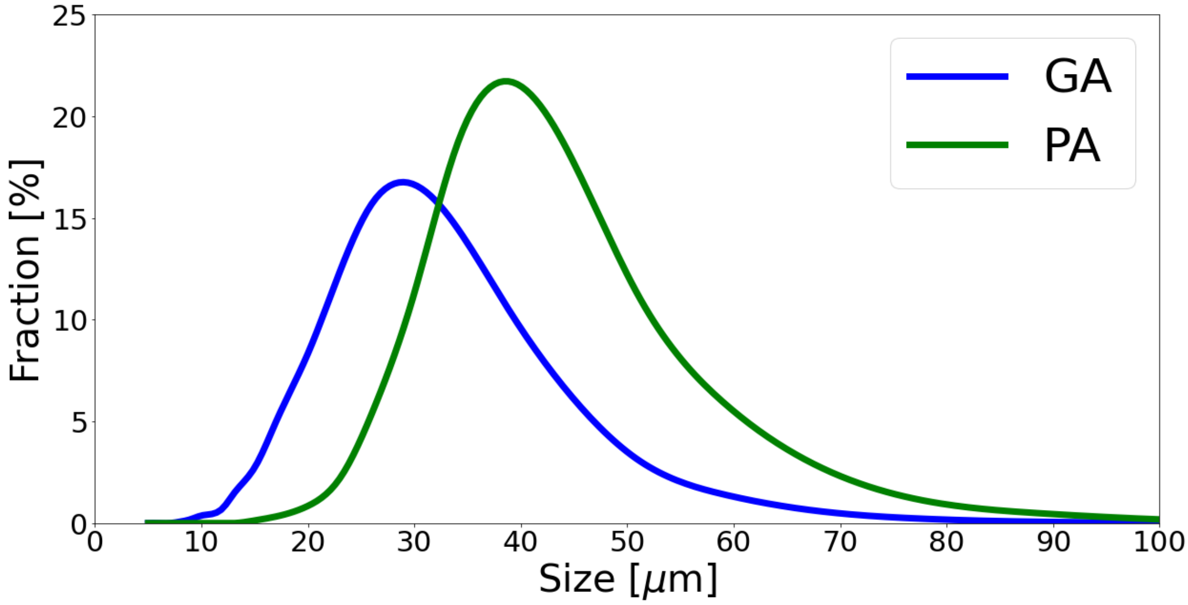

Figure 4. Average particle size distributions of the virgin GA and PA powders
Abbreviations: GA: Gas-atomized; PA: Plasma-atomized.

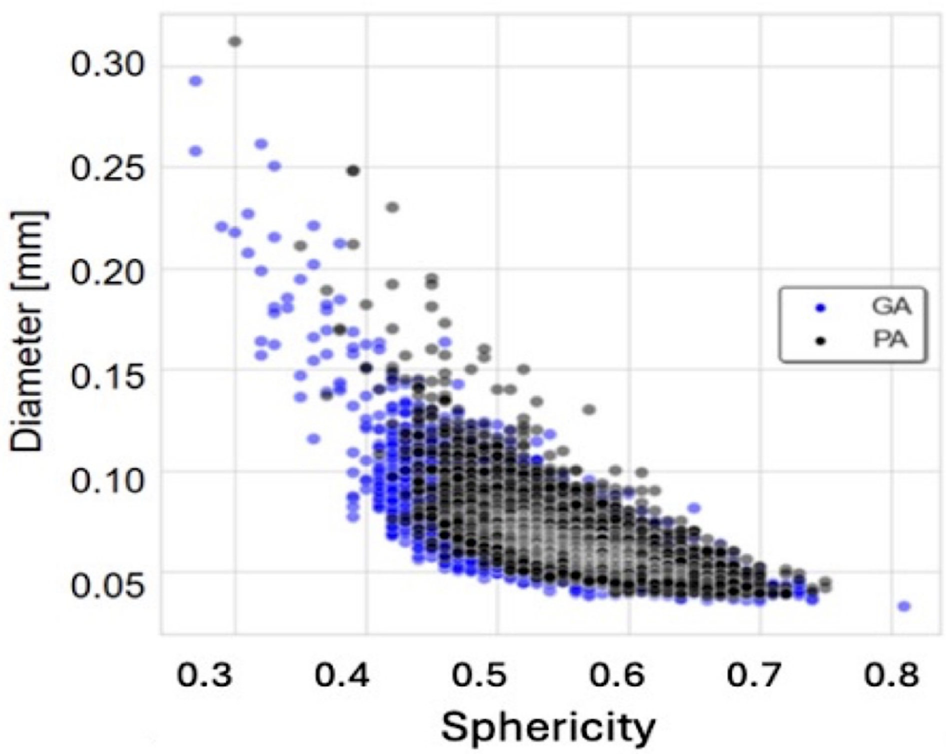

Figure 5. Size distribution of pore size and pore sphericity of the metal from all specimens in the first build for the GA and PA powder
Abbreviations: GA: Gas-atomized; PA: Plasma-atomized.

3.3. Mechanical properties

The average YS, UTS, strain at failure, and tensile toughness of the specimens with vertical and horizontal orientations are summarized in Table 3; the coefficient of variation (COV) is also provided for each of the properties for comparison. The values in this table represent the average of metal properties from all builds. As evident from these values the average YS and UTS of metal from the GA powder were lower than that of its PA counterpart by approximately 10% (these differences were significant ($p \leq 0.05$)). However, there was no significant difference in the average strain at failure or tensile toughness between the metal produced with GA and PA powders. Regarding the variation in mechanical properties, the COV values for the YS and UTS are similar, and <3% for both for GA and PA powders. However, the metal produced with GA powder exhibited larger COV in the strain at failure and tensile toughness than those for the PA powder, especially for the vertically printed specimens. The metal produced from both powders exhibited greater variation in the strain at failure and tensile toughness than in the measures of strength (YS and UTS), which is attributed primarily to the variation in ductility.

The material data sheet for the vertical orientation of the PA powder reports a yield and ultimate tensile strength of 1010 MPa and 1080 MPa, respectively, and strain to failure of 15%. As evident from the values in Table 3, the metal strength achieved with the PA powder exceeded that performance; the strain to failure for the vertical orientation is lower than that in the data sheet but approaching the expected value. A materials data sheet was not provided for the experimental GA powder. Nevertheless, results for the measures of strength for the vertical orientation produced with the GA powder are approaching the value reported in the PA standard (*i.e.*, both are within ≤3% of the data sheet); the measures of strain are lower than the data sheet values, which could be attributed to the absence of process parameter optimization performed with this powder. However, results for the strain to failure of the horizontal orientation are substantially lower than defined in the data sheet, for both the GA and PA powders.

In consideration of potential changes in the mechanical properties with build number, the YS and the UTS for the metal obtained from the two different powders are shown in Figure 6a and 6b, respectively. Similarly, the strain to fracture and tensile toughness are shown in Figure 6c and 6d, respectively. Overall, the degree of variation in tensile strength of the metal produced with the two powders is limited, exhibiting no clear trend with powder reuse through the six builds. This suggests that there is no appreciable degradation in the powder quality over the build cycles. As expected from the average values in Table 3, the metal produced with GA powder exhibits lower YS and UTS than those values for the PA powder regardless of build number and print orientation. However, there is more notable variation in the measures of strain to failure and toughness. Interestingly, the strain at failure and toughness are primarily dependent on the orientation of metal as opposed to which powder is used. The horizontal orientation exhibits the lowest strain at failure and toughness, regardless of powder used for the build, as well as the larger degree of variation as evident from the number of outliers in the measures of ductility of the specimen.

The mechanical properties were also examined according to build zone to reflect the possible spatial variations related to effects of laser distortion, recoater sweeping, gas flow, *etc.* The YS and UTS of both horizontal and vertical samples are presented in Figure 7a and Figure 7b, respectively. Interestingly, the metal built at the center of the build plate (Zone A0) shows the highest strength overall with respect to the other zones, and there is an apparent decrease in strength with zone. The metal from Zone A4 exhibits the relative lowest values of YS and UTS. When examined in this manner, the spatial variations in properties appear more pronounced in the metal produced with GA than the PA powder. Additionally, it is noteworthy that the variation in strength of metal produced with GA powder is greatest in Zones 3 and 4. Based on the distributions in Figure 7c and 7d, there is no zonal variation in ductility in either the vertical or horizontal samples. Nevertheless, the metal with horizontal orientation exhibits lower ductility and less variation than that evident from metal with vertical orientation for both powder sources.

Weibull probability plots for selected properties are shown in Figure 8. The distributions in UTS for the vertical and horizontal specimens are shown in Figure 8a for metal printed with the GA and PA powder. Results for the UTS distribution are largely non-linear, particularly for the PA powder, suggesting that the Weibull weakest link model may not be appropriate. The UTS distribution for the metal produced with the GA powder exhibits a bimodal response, suggesting that the strength is primarily a function of two predominant families of microstructural defects. The UTS distribution for the horizontal metal exhibits the highest Weibull modulus of the responses overall.

The Weibull distributions for the strain at failure measurements are shown in Figure 8b. Compared to the UTS, the strain at failure distributions are predominantly unimodal and exhibit a greater degree of linearity. Furthermore, these results show the greater importance

Table 3. Overall mechanical properties from pooled results of all six builds in terms of the mean ± standard deviation and coefficient of variation (%)

	Powder source	YS (MPa)	UTS (MPa)	Strain at failure (mm/mm)	Tensile toughness (MPa)
Vertical	GA	1003 ± 28 (2.79%)	1052 ± 30 (2.87%)	0.12 ± 0.020 (16.34%)	118 ± 19 (16.40%)
	PA	1103 ± 23 (2.08%)	1142 ± 21 (1.86%)	0.12 ± 0.015 (12.90%)	128 ± 16 (12.54%)
Horizontal	GA	1019 ± 23 (2.22%)	1075 ± 22 (2.08%)	0.09 ± 0.008 (9.42%)	91 ± 11 (12.46%)
	PA	1116 ± 16 (1.44%)	1164 ± 15 (1.33%)	0.08 ± 0.007 (9.21%)	90 ± 8 (9.23%)

Abbreviations: GA: Gas-atomized; PA: Plasma-atomized; UTS: Ultimate tensile strength; YS: Yield strength.

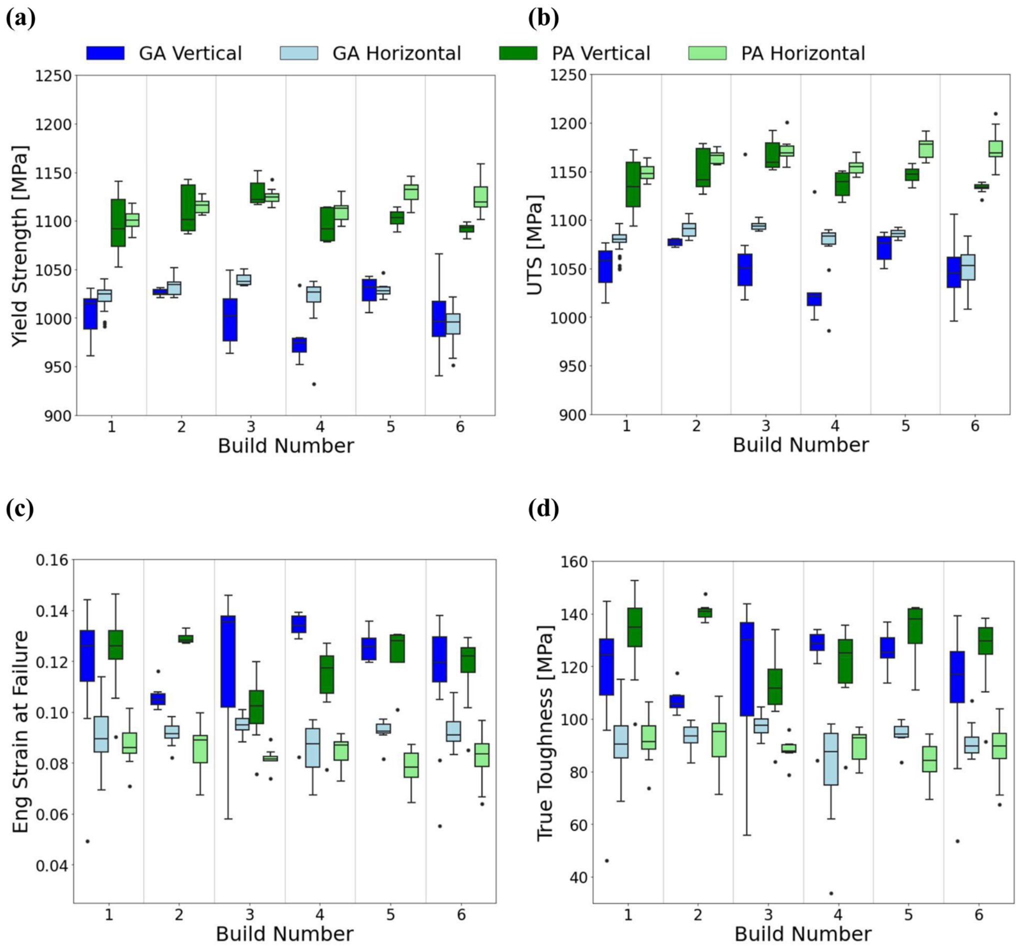

Figure 6. Overall results from uniaxial testing of the metal built with the GA and PA powders presented with respect to the build number. (a) Yield strength, (b) ultimate tensile strength, (c) engineering strain at failure, (d) tensile toughness. The box and whisker plots for each zone represent the median, first and third quartiles, the upper and lower limits, and the outliers.
Abbreviations: GA: Gas-atomized; PA: Plasma-atomized.

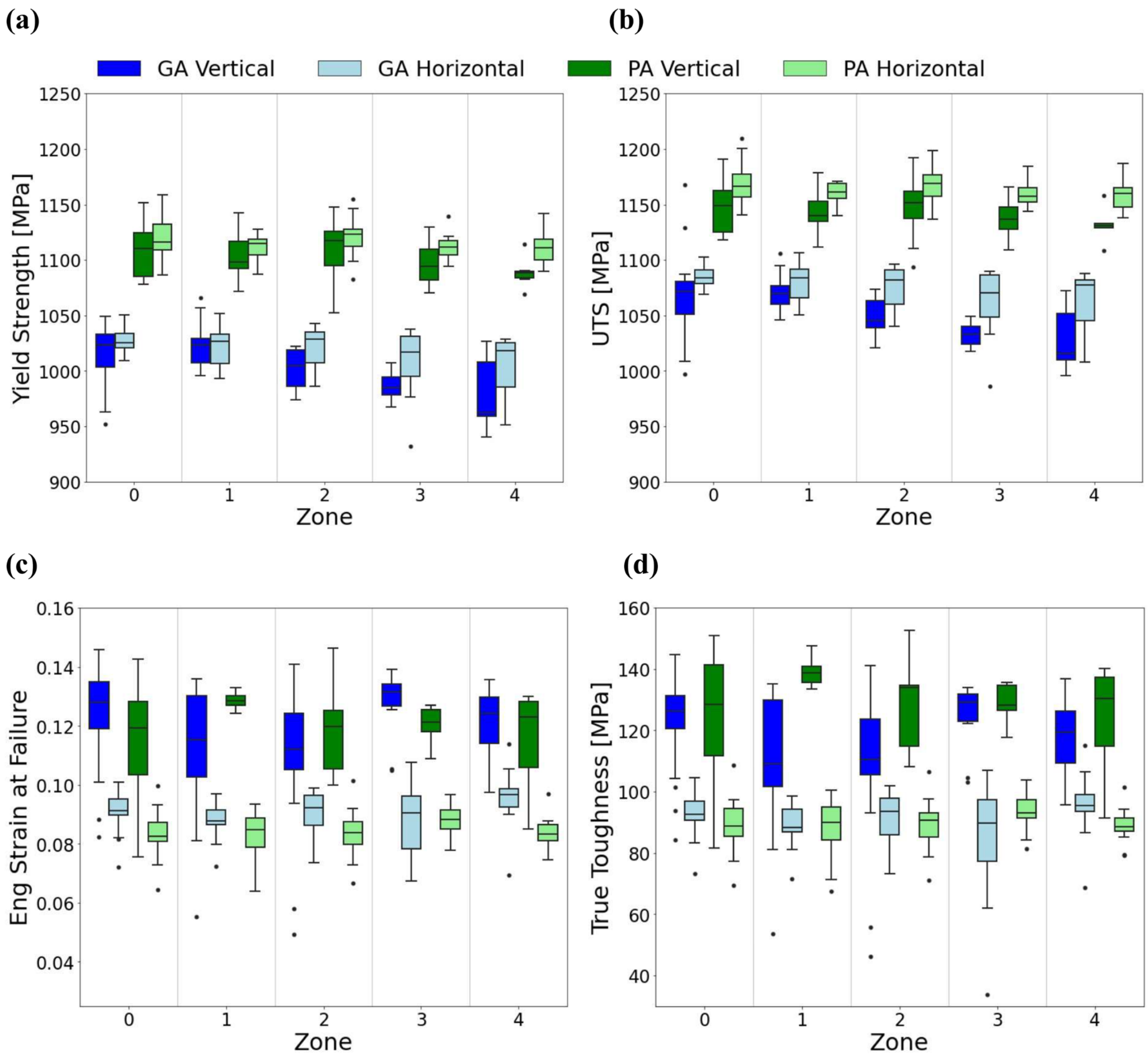

Figure 7. Overall results from uniaxial testing of the metal printed with GA and PA powder from Level A presented in terms of the build zone as shown in Figure 1. (a) Yield strength, (b) ultimate tensile strength, (c) engineering strain at failure, (d) tensile toughness. The box and whisker plots for each zone represent the median, first and third quartiles, the upper and lower limits, and the outliers.
Abbreviations: GA: Gas-atomized; PA: Plasma-atomized.

of metal orientation on the strain to failure than powder. For the specimens built with vertical orientation, the distributions and Weibull moduli for the PA and GA powder are nearly identical, suggesting limited dependence on the powder type. It is important to note that the specimens with vertical orientation exhibit a substantially larger range in strain to failure than exhibited by the horizontal samples. Interestingly, the GA samples with horizontal orientation exhibit greater strain to failure and larger consistency in the responses than the PA samples as distinguished from the Weibull moduli.

3.4. Fractography

Fractography was performed on the fractured tensile specimens to further understand contributions to the mechanical properties. All fractures took place within the gage length. A variety of features were visible to the unaided eye, such as voids, cavities and differences in surface texture. The fractures surfaces were investigated in more detail to distinguish typical features of the fracture morphology for the experimental groups and the root causes. Guided by a combination of the tensile data and the identification of apparent defects, selected samples were chosen for further analysis by SEM and digital quantitative microscopy.

Macroscopically, most coupons displayed characteristic ductile failure morphology with clear necking about the region of fracture as shown in Figure 9 and prominent shear lips, which are expected from the measures of strain at failure. There was also substantial evidence of plastic deformation at higher magnification as outlined in the SEM views in Figure 9. The fracture characteristics showed equiaxed dimples in the central region of the fracture surface and parabolically shaped dimples in the region of the shear lips. These characteristics were evident in all specimens evaluated. Hence, despite the defects revealed on the fracture surfaces, failure occurred through ductile overload of the prismatic section.

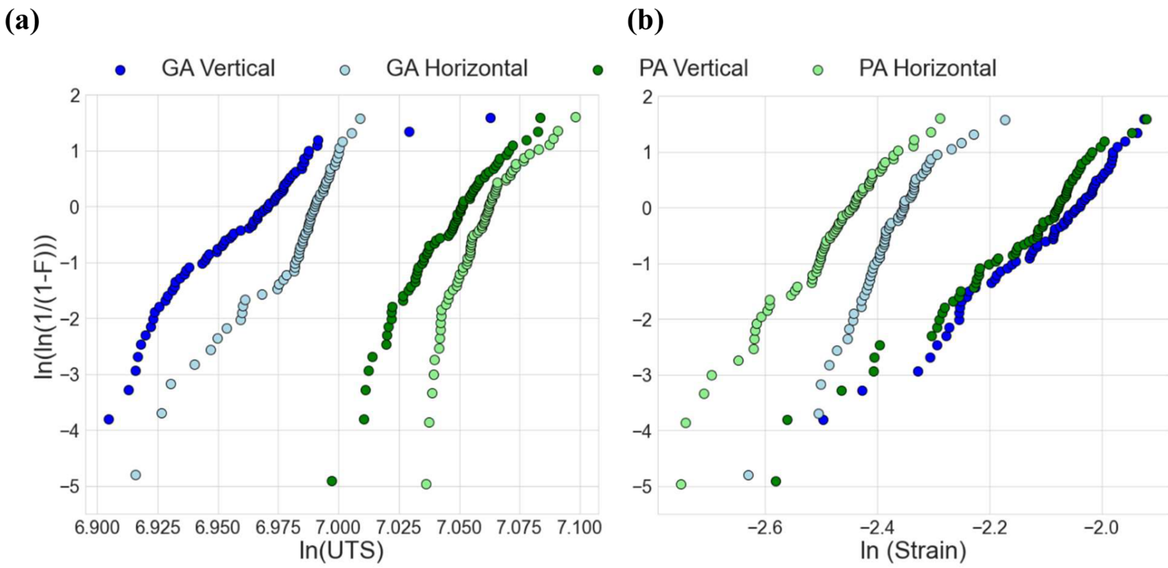

Figure 8. Weibull distributions for (a) the ultimate tensile strength (MPa) and (b) engineering strain at failure (mm/mm) of metal produced with the GA and PA powders
Abbreviations: GA: Gas-atomized; PA: Plasma-atomized.

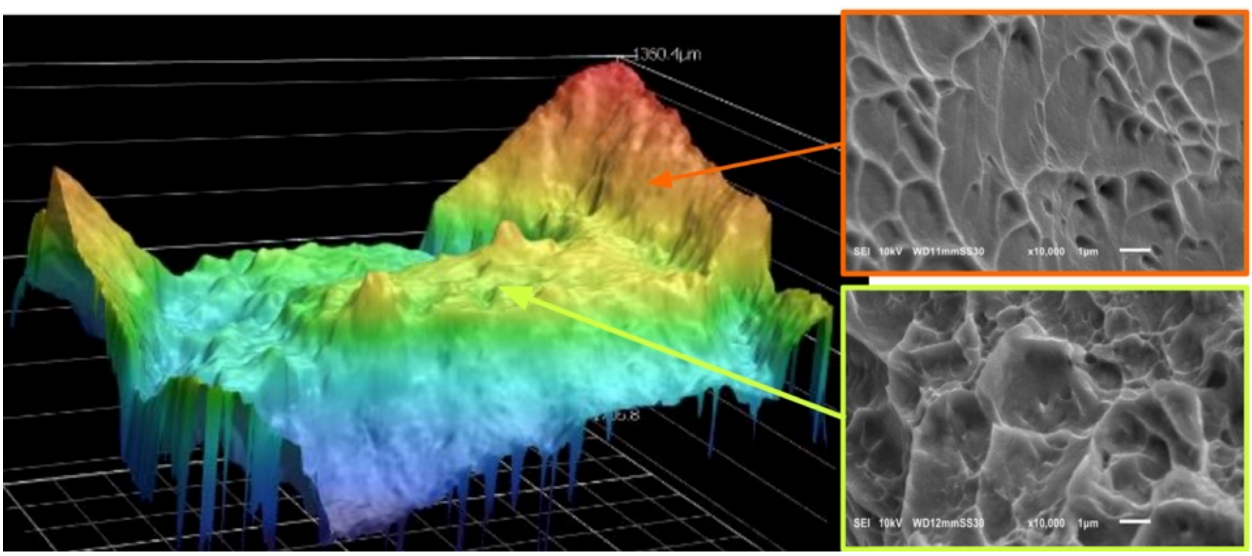

Figure 9. Oblique view of a fracture surface from a typical gas-atomized (GA) metal specimen with highlight of microvoid coalescence that was present in the different regions of the fracture surface. Magnification of scanning electron micrographs = 10,000×.

In addition to the characteristic ductile failure characteristics, voids were evident on the fracture surfaces, as shown for representative samples produced with GA powder in Figure 10. These fracture surfaces were imaged further to obtain high-resolution views of important features of the surface morphology. Specifically, Figure 10 shows the fracture surfaces of two specimens of interest via optical microscopy, as well as complementary views of the voids at higher magnification using SEM. Both exhibit LOF voids on the fracture surface, with powder particles evident within the void when examined at higher magnification.

4. Discussion

Although the metal printed with GA powder was produced using the identical machine and process parameters, followed the same build design as used for the PA powder, and was subjected to the identical heat treatment, it had lower tensile strength for both orientations. In addition, the metal produced with GA powder exhibited substantially wider spatial variations across the build plate than that produced using the PA powder as shown in Figure 7b. Hence, while the differences in powder properties appeared rather limited, they played an important role on the quality of metal produced.[65] Of note, differences in metal produced with the two powders was reflected in the strength distributions, but not in the strain at failure or tensile toughness.

Results of the Weibull distributions in Figure 8 were used to pursue additional understanding of the root causes and contributing defects to failure through a complementary fractographic analysis. Specifically, the five specimens with highest and lowest strain to failure were scanned using digital microscopy. Results for the metal built with GA powder and with vertical orientation are shown in Figure 11a**.** Corresponding results for metal printed with the horizontal orientation are shown in Figure 11b.

Regarding the detailed views in Figure 11a, there is a correlation between the macroscopic fracture surface characteristics and the probability of failure. Failures corresponding to low strain and located in the tail of the statistical distribution more frequently initiated at the surfaces of the specimens, which is evident from the intersection of the flat aspect of the fracture surface with the specimen surface, coincident with the plane of maximum normal stress. Despite the comparatively low strain at failure, these were ductile failures that generated extensive shear lips at overload. In contrast, specimens with

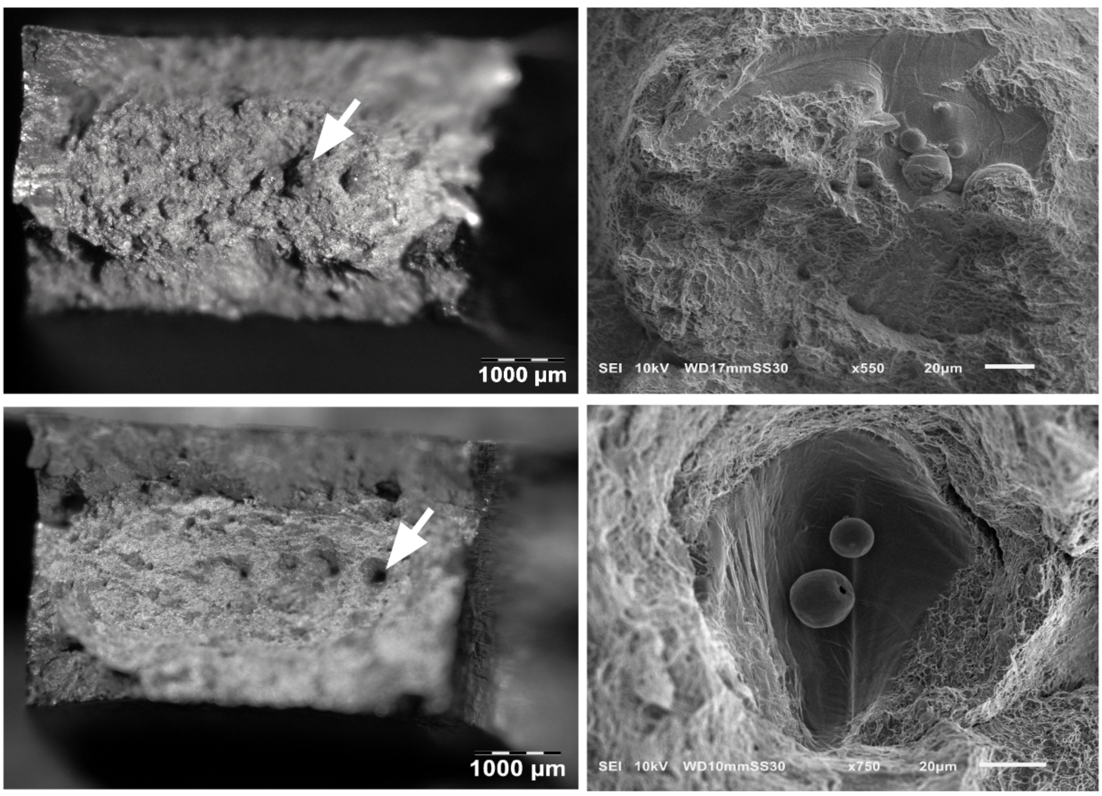

Figure 10. Internal lack of fusion voids on the fracture surface of selected tensile specimens with vertical orientation produced using GA powder

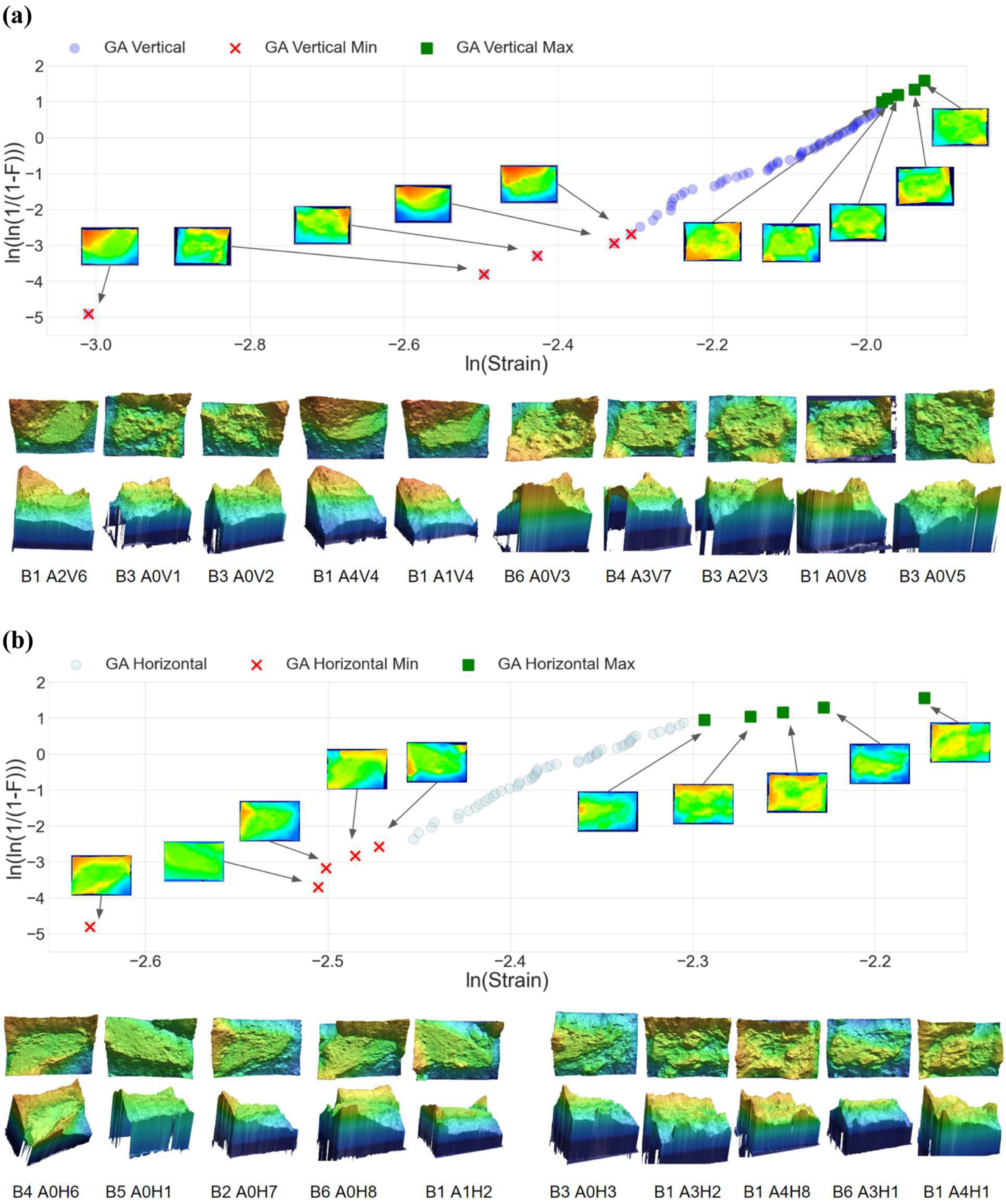

Figure 11. Evaluation of the failure distribution extrema for the metal printed with gas-atomized (GA) powder as distinguished from the Weibull distributions and the corresponding fracture surface profiles as documented using digital microscopy. Note that the nominal gage-section dimensions are 6 × 4.5 mm for all specimens. (a) Vertical orientation. The specimen with lowest strain at failure was in Zone 2 of Build 1. (b) Horizontal orientation. The specimen with lowest strain at failure was in Zone 0 of Build 4. All strain measures listed in terms of mm/mm. The specimen ID below the fracture distinguishes the build (B1-B6), the level and zone (A1 to A5), and the specimen orientation and placement (V1-V10 or H1-H9).

the highest strain at failure exhibited fracture surfaces with larger central region, a manifestation of void coalescence, and oriented parallel to the plane of maximum normal stress. A review of these fracture surfaces using optical microscopy showed that these fracture surfaces were substantially rougher than those with low failure strains, undoubtedly a function of the extensive deformation to failure. Therefore, while no correlation was found between the pore morphology and the strength, there was a tendency for failures initiated at surface notches to result in lower strain to failure. For the vertical specimens, these defects were LOF voids that were relieved by machining. The absence of a strong correlation is due to the mode of loading, which consisted of quasistatic loading to failure. The ductile characteristics of the Ti6Al4V reduces the effective stress concentration of the notch root through inelastic deformation. A much stronger relationship between void location, their morphology and the fatigue behavior of metal from the PA and GA powders is expected.

For the horizontal orientation shown in Figure 11b, the observations were largely consistent with the vertical orientation in Figure 11a. Failures corresponding to the tail of the distribution also initiated at the surface of the specimens, which is evident from the topography maps in this figure, and with fracture plane orientation coincident with the plane of maximum principal stress. In contrast, the fracture surface of specimens with the largest strain at fracture exhibited a larger central region with tortuous topography resulting from the extensive deformation. Despite the differences, all the fracture surfaces exhibited prominent shear lips. These observations were consistent for the PA metal.

The GA powder had a wider particle size distribution when compared to the PA powder (Figure 3), which leads to less uniformity in laser absorption.[36,66] As such, the process parameters used for the two powders and laser power settings could be insufficient for the GA powder, leading to more LOF voids between build layers. Although speculative, the statement is supported by the X-ray computed microtomography data reflecting the greater number of lack of fusion voids in the metal produced with GA powder and lower sphericity in Figure 5. The greater number of small and satellite particles of the GA powder, evident in Figures 3 and 4, could result in less efficient heating and melting, increasing the likelihood of spatter emission and the probability of interlayer defects.[67,68] Those characteristics also appeared to reduce flowability and packing density and would be expected to reduce the powder bed thermal conductivity. However, results from the recent work of Meier *et al.*[54] suggest that the difference in particle size alone between the GA and PA powders is less likely a contributing factor to the performance differences. Rather, it is more likely a result of the combined effect of the lower sphericity and larger volume fraction of small particles in the GA powder (Figure 4), and greater number of satellites (Figure 3), all of which contribute to lower spreadability.[69] Potential disruptions in the energy absorption due to reduced powder spreadability is plausible and is highlighted by the pore concentration and sphericity distribution in Figure 5.

Fractographic evaluation of the samples revealed that LOF defects were more commonly found on the fracture surfaces of the metal produced with GA powder. Admittedly, the location of pores in the metal as well as the size can greatly contribute to the mechanical properties and the interpretation of contributions from the two powder sources. Nevertheless, these findings agree with those of Ruan *et al.*[28] comparing builds performed with GA vs PA powders of Inconel, which showed that some of the issues can be address by optimizing laser speed and power.

There were differences in the inherent quality of the powders that are important to consider, including defects and morphology. Figure 3 shares examples of internal gas pores and peripheral satellites, which were more commonly noted in evaluating the virgin GA powder and could contribute to porosity. The greater number of smaller particles and the irregular shapes in comparison to the PA powder increases the likelihood of static interactions. This impacts the flowability of the virgin powder, which made the standard flowability measurements with the GA powder difficult or impossible. The lack of uniformity in powder size and shape hindered even mixing of powders in the powder keg, influencing its spreadability on the build plate.[70] Furthermore, a larger fraction of small particles in the GA powder makes the generation of spatter more likely and contributes to greater likelihood of dispersion stimulated by the gas flow. Further investigations into the impact of gas flow on the powder dynamics and mechanical properties of the metal are warranted.

As evident from the quantitative measure of particle size distributions (Tables A3 and A4) the properties of the GA powder remained largely constant throughout all six builds, except for the angle of repose, which underwent a small decrease in the last two builds. Degradation of the powder was not expected due to the limited number of reuse cycles and is consistent with results of previous studies.[15,19,28,31,71] Interestingly, the GA powder did appear to undergo an increase in relative flowability with reuse, as noted from the ability to perform Hall Flow measurements that were previously flow-limited. It is expected that the reduction of satellites as well as the fine and large particles removed during the sieving processes reduced the static friction in particle-particle interactions, which increased flowability.[72] Nevertheless, based on the responses in Figure 6, there was no difference in the apparent aging of the GA and PA powders over the builds that resulted in an evolution of properties with reuse.

Akin to the absence of changes in powder quality with build number, there were no significant changes in the mechanical properties of the metal with build number for either the GA or PA powders. It is possible that changes in powder potentially had not yet manifested due to the limited number of reuse cycles or were not significant enough to be reflected on the mechanical properties. However, there were some differences in mechanical properties with respect to build zones as shown in Figure 7b, which were most evident in the metal produced with GA powder in comparison to that with the PA powder. Specifically, the results showed significant ($p \leq 0.05$) differences in the strength of metal in Zone A4, near the back corner of the EOS M290. While the differences in strength were apparent for both specimen orientations, they appeared most prominent for the vertical orientation, as expected. The vertical orientation should be most sensitive to LOF defects due to their orientation relative to the maximum principal stress. A recent investigation regarding the gas flow distribution in the M290 showed that there are spatial variations across the build plate.[73] The back of the machine, near the powder inlet (*i.e.*, nearest Zones 1 and 4) exhibited the greatest deviation from uniformity, which agrees with the mechanical property distribution.

One of the most valuable findings from fractography guided by the Weibull distributions for the strain at failure is the correlation between defect location and degradation in mechanical properties. The tensile specimens with lowest strain at failure all exhibited failure origins located at the surface of the sample, as shown in Figure 11b. The primary printing anomalies, including LOF voids located at or near the surface, posed stress concentrations that were more detrimental than the internal pores. In general, surface pores are the most difficult to identify by tomography,[74] and they are equally difficult to identify by surface texture analysis. Due to the distortion that arises from the strain to failure, it was often not possible to identify the root cause defect or synergistic defects when failure did not initiate from the surface. As such, weighting of the contributions from LOF and gas pores to the initiation of failures was not possible. Nevertheless, most pores contributing to the tensile behavior appeared to be the LOF voids due to their larger size. Failures were not identified that occurred due to gas pores and it was not possible to ascertain if the gas pores were residual internal pores from the powder or from interactions between the laser and powder.

The differences between results for the vertical and horizontal orientation in Figure 11 are expected to be a result of the pore orientation and its alignment with the opening mode stress field. The failure origins for the horizontal specimens appeared more related to the pore size than the pore location, which is related to the reduced importance of the LOF voids on the initiation of failure This trend would be present regardless of powder type.

In summary, the results of this investigation showed that the metal produced with GA powder exhibited lower strength than that produced with the PA powder, and that the builds performed with GA powder exhibited a larger degree of spatial variation in the tensile properties across the build plate. The latter suggests that build design and layout is more important if GA powder is used and that the metal would exhibit lower reliability if further post-processing (*e.g.*, hot isostatic pressing) is not performed. Overall, the findings suggest that if metal reliability is a key metric, GA powder should not be used in place of PA powder and/or if further post-processing is not applied. It is important to note that the builds performed with the PA and GA powders utilized the default process parameters for the PA powder, as outlined in the Methods section. An optimization of the process parameters was not performed for either powder as it was not within the program scope. A separate process optimization, specifically for the GA powder, could potentially improve the metal quality and should be considered in future studies.

Despite the importance of the findings of this investigation, there are limitations to the work that should be considered beyond that related to powder-specific process optimization. One concern is that the evaluation did not include a detailed assessment of the grain structure and differences of phases of the metal from the GA and PA powder, including the prior beta grains and the alpha lath dimensions. That information could provide further understanding of the fundamental mechanisms contributing to differences in ductility between the metal produced with the two powders and the contributions to variability beyond the contribution of voids; the effects of microstructure and process defects are undoubtedly combinatorial. Hence, this is recommended for future work. Nevertheless, the differences in size and aspect ratio of defects in the metal produced with the two powders provided sufficient understanding to discontinue further consideration of the GA powder. Of relevance, the evaluation was conducted on the metal after a stress-relief heat treatment only. It is possible that hot isostatic pressing (HIP) could change the level of anisotropy, as well as the differences in performance of the GA and PA metal through a reduction in flaw size and pore count.[75,76]

Another concern relates to the difference in the build height performed with the PA and GA powders. Due to the experimental nature of the GA powder, it was not possible to secure a sufficient volume to complete the full build height to the B level as with the PA powder. Printing was performed with the PA powder before securing the GA powder. One alternative to consider for future work, which was not performed in the present study, could include performing the builds with PA powder to half height. Here, the PA powder had already gone through six build cycles, and performing additional builds at half height (*i.e.*, A level only) would involve powder with a greater extent of reuse. Due to the degree of physical separation between the A and B levels, no differences in the results are expected in the tensile properties related to build height with the PA and GA powders.[77] Nevertheless, it is a limitation of this investigation. To minimize the potential influence of build level, the comparison of properties was only conducted with metal from the A level for both the PA and GA powders. Additionally, while the GA and PA powders had similar size distributions; the GA powder had more satellites (Figure 3), smaller average diameter and lower sphericity (Figure 4). According to Xue *et al.*[78], minimal differences in tensile properties are expected from the difference in particle size distribution. However, Brika *et al.*[79] reported that higher number of fines and lower sphericity of GA powder reduces flowability and results in lower strength, which is consistent with the findings of the present study. Of note, the two studies used the same stress relief temperature of 800 °C, but there were differences in time, which can contribute to the unique results. Lastly, the comparison of mechanical behavior did not include fatigue, which is more sensitive to microstructure and defects. As such, the present study should be considered the first phase of evaluation. Despite these concerns, this investigation further establishes the relative merits of L-PBF with PA and GA powders and makes an important contribution that advances industrialization of L-PBF for stress-critical applications.

5. Conclusion

Laser powder bed fusion (L-PBF) was performed with gas-atomized (GA) and a comparable plasma-atomized (PA) powder of Grade 5 Ti6Al4V to assess the differences in quality and mechanical properties of the metal produced. The objective was to distinguish whether GA powder could be used as a lower cost substitute without sacrifices in performance. Based on results of the experimental evaluation, the following conclusions are drawn:

(i) The virgin GA powder particles were less spherical than the PA powder, had smaller average particle size, and wider distribution in comparison to the PA powder, which reduced the flowability over the build plate.
(ii) The yield and ultimate tensile strength (UTS) of the metal produced with GA powder were approximately 10% lower than those achieved with the PA powder for both the vertical and horizontal orientations.
(iii) Based on six build cycles performed with each powder, there was no significant change in mechanical properties of the material with reuse in terms of UTS and strain to failure.
(iv) While there were limited changes in mechanical properties with powder reuse, the GA powder exhibited more prominent spatial variations in the tensile strength. Samples built in the central zone directly beneath the laser source displayed the best mechanical response, whereas the samples built closest to the recoater blade parked position and gas flow inlet displayed the lowest UTS.
(v) The fracture surfaces showed that lack of fusion voids were the primary contributions to the distribution in mechanical properties. Future studies should be performed to determine if post-processing, such as hot isostatic pressing, could further homogenize the properties of GA-printed metal to the level of PA-printed metal.

Acknowledgments

The authors would like to thank Eric Chapman and Stacey Huang of the Boeing Company for their technical discussions and guidance.

Funding

The authors gratefully acknowledge that support for this investigation was received from The Boeing Company through the Boeing Advanced Research Collaboration. Partial support was also received from the Federal Aviation Administration through the Center of Excellence for Advanced Materials in Transport Aircraft Structures (AMTAS). Part of this work was supported by the Washington Nanofabrication Facility/Molecular Analysis Facility, a National Nanotechnology Coordinated Infrastructure (NNCI) site at the University of Washington with partial support from the National Science Foundation via awards NNCI-1542101 and NNCI-2025489.

Conflict of interest

Dwayne D. Arola serves as the Associate Editor of this journal, but was not in any way involved in the editorial and peer-review process conducted for this paper, directly or indirectly. The authors have no conflicts of interest to declare.

Author contributions

Conceptualization: Cory Cunningham, Reid Schur, Mamidala Ramulu, Dwayne Arola
Formal analysis: Jordan Hatch, Alex Hicker, Chris Liu, Alex Montelione
Investigation: Jordan Hatch, Alex Hicker, Chris Liu, Alex Montelione
Methodology: Alex Montelione, Reid Schur, Mamidala Ramulu, Dwayne Arola
Writing–original draft: Jordan Hatch, Alex Hicker, Chris Liu, Alex Montelione
Writing–review & editing: Reid Schur, Cory Cunningham, Mamidala Ramulu, Dwayne Arola

Ethics approval and consent to participate

Not applicable.

Consent for publication

Not applicable.

Availability of data

Data are available from the corresponding author upon reasonable request.

References

1. Natarajan J. *Advances in Additive Manufacturing Processes*. Bentham Science Publishers; 2021.

2. Hajare DM, Gajbhiye TS. Additive manufacturing (3D printing): Recent progress on advancement of materials and challenges. *Mater Today Proc*. 2022;58(2):736.

   doi: 10.1016/j.matpr.2022.02.391

3. Wimpenny DI, Pandey PM, Kumar LJ, editors. Advances in 3D printing & additive manufacturing technologies. Singapore: Springer; 2017.

4. Vafadar A, Guzzomi F, Rassau A, Hayward K. Advances in Metal Additive Manufacturing: A Review of Common Processes, Industrial Applications, and Current Challenges. *Appl Sci.* 2021;11(3):1213.

   doi: 10.3390/app11031213

5. Goh GD, Yap YL, Agarwala S, Yeong WY. Recent Progress in Additive Manufacturing of Fiber Reinforced Polymer Composite. *Adv Mater Technol*. 2018;4(1):1800271.

   doi: 10.1002/admt.201800271

6. Cao S, Zou Y, Lim CVS, Wu X. Review of laser powder bed fusion (LPBF) fabricated Ti-6Al-4V: process, post-process treatment, microstructure, and property. *LAM*. 2021;2(2):1.

   doi: 10.37188/lam.2021.020

7. Cabrini M, Carrozza A, Lorenzi S, *et al.* Influence of surface finishing and heat treatments on the corrosion resistance of LPBF-produced Ti-6Al-4V alloy for biomedical applications. *J Mater Process Technol*. 2022;308:117730-117730.

   doi: 10.1016/j.jmatprotec.2022.117730

8. Gupta A, Bennett CJ, Sun W. High Cycle Fatigue Performance Evaluation of a Laser Powder Bed Fusion Manufactured Ti-6Al-4V Bracket for Aero-Engine Applications. *Eng Fail Anal*. 2022;140:106494.

   doi: 10.1016/j.engfailanal.2022.106494

9. Su JL, Jiang FL, Teng J, *et al.* Laser additive manufacturing of titanium alloys: process, materials and post-processing. *Rare Metals*. 2024:43(12): 6288-6328.

   doi: 10.1007/s12598-024-02685-x

10. Blakey-Milner B, Gradl P, Snedden G, *et al.* Metal additive manufacturing in aerospace: A review. *Mater Des*. 2021;209(1):110008.

    doi: 10.1016/j.matdes.2021.110008

11. Yusuf SM, Cutler S, Gao N. Review: The Impact of Metal Additive Manufacturing on the Aerospace Industry. *Metals*. 2019;9(12):1286.

    doi: 10.3390/met9121286

12. Taminger KM, Domack CS. Challenges in Metal Additive Manufacturing for Large-Scale Aerospace Applications. *Women Aerosp Mater.* 2020;105-124.

    doi: 10.1007/978-3-030-40779-7_8

13. Montelione A, Ghods S, Schur R, Wisdom C, Arola D, Ramulu M. Powder Reuse in Electron Beam Melting Additive Manufacturing of Ti6Al4V: Particle Microstructure, Oxygen Content and Mechanical Properties. *Addit Manuf*. 2020;35:101216.

    doi: 10.1016/j.addma.2020.101216

14. Ghods S, Schultz E, Wisdom C, *et al.* Electron beam additive manufacturing of Ti6Al4V: Evolution of powder morphology and part microstructure with powder reuse. *Materialia*. 2020;9:100631.

    doi: 10.1016/j.mtla.2020.100631

15. Soundarapandiyan G, Johnston C, Khan RHU, *et al.* The effects of powder reuse on the mechanical response of electron beam additively manufactured Ti6Al4V parts. *Addit Manuf*. 2021;46:102101.

    doi: 10.1016/j.addma.2021.102101

16. Tang HP, Qian M, Liu N, Zhang XZ, Yang GY, Wang J. Effect of Powder Reuse Times on Additive Manufacturing of Ti-6Al-4V by Selective Electron Beam Melting. *JOM*. 2015;67(3):555-563.

    doi: 10.1007/s11837-015-1300-4

17. Derimow N, Gorham JM, Martin ML, Benzing JT, White RM, Hrabe N. Surface chemistry in Ti-6Al-4V feedstock as influenced by powder reuse in electron beam additive

manufacturing. *Appl Surf Sci*. 2022;602:154280.

doi: 10.1016/j.apsusc.2022.154280

18. Gruber H, Henriksson M, Eduard Hryha, Nyborg L. Effect of Powder Recycling in Electron Beam Melting on the Surface Chemistry of Alloy 718 Powder. *Metall Mater Trans A Phys Metall Mater Sci*. 2019;50(9):4410-4422.

doi: 10.1007/s11661-019-05333-7

19. Quintana OA, Alvarez J, Mcmillan R, Tong W, Tomonto C. Effects of Reusing Ti-6Al-4V Powder in a Selective Laser Melting Additive System Operated in an Industrial Setting. *JOM*. 2018;70(9):1863-1869.

doi: 10.1007/s11837-018-3011-0

20. Soltani-Tehrani A, Isaac JP, Tippur HV, Silva DF, Shao S, Shamsaei N. Ti-6Al-4V powder reuse in laser powder bed fusion (L-PBF): The effect on porosity, microstructure, and mechanical behavior. *Int J Fatigue*. 2023;167:107343.

doi: 10.1016/j.ijfatigue.2022.107343.

21. Zhuo Z, Ji R, Wang L, Mao J. Reusability of Ti-6Al-4V powder in laser powder bed fusion: Influence on powder morphology, oxygen uptake, and mechanical properties. *J Mater Processing Technol*. 2025;335:118672.

doi: 10.1016/j.jmatprotec.2024.118672

22. Harkin R, Wu H, Nikam S, *et al.* Powder reuse in laser-based powder bed fusion of Ti6Al4V—changes in mechanical properties during a powder top-up regime. *Materials*. 2022;15(6):2238.

doi: 10.3390/ma15062238

23. Meier B, Warchomicka F, Ehgartner D, *et al.* Toward a sustainable laser powder bed fusion of Ti 6Al 4 V: Powder reuse and its effects on material properties during a single batch regime. *Sustain Mater Technol*. 2023;36:e00626.

doi: 10.1016/j.susmat.2023.e00626.

24. Carrion PE, Soltani-Tehrani A, Phan N, Shamsaei N. Powder Recycling Effects on the Tensile and Fatigue Behavior of Additively Manufactured Ti-6Al-4V Parts. *JOM*. 2019;71(3):963-973.

doi: 10.1007/s11837-018-3248-7

25. Chen G, Zhao SY, Tan P, Wang J, Xiang CS, Tang HP. A comparative study of Ti-6Al-4V powders for additive manufacturing by gas atomization, plasma rotating electrode process and plasma atomization. *Powder Technol*. 2018;333:38-46.

doi: 10.1016/j.powtec.2018.04.013

26. Xie B, Fan Y, Zhao S. Characterization of Ti6Al4V powders produced by different methods for selective laser melting. *Mater Res Express*. 2021;8(7):076510-076510.

doi: 10.1088/2053-1591/ac10d1

27. Kassym K, Perveen A. Atomization processes of metal powders for 3D printing. *Mater Today Pro*. 2020;26:1727-1733.

doi: 10.1016/j.matpr.2020.02.364

28. Ruan G, Liu C, Qu H, *et al.* A comparative study on laser powder bed fusion of IN718 powders produced by gas atomization and plasma rotating electrode process. *Mater Sci Eng A*. 2022;850:143589-143589.

doi: 10.1016/j.msea.2022.143589

29. Moghimian P, Poirié T, Habibnejad-Korayem M, *et al*. Metal powders in additive manufacturing: A review on reusability and recyclability of common titanium, nickel and aluminum alloys. *Addit Manuf*. 2021;43:102017.

doi: 10.1016/j.addma.2021.102017

30. Lagutkin S, Achelis L, Sheikhaliev SM, Volker Uhlenwinkel, Srivastava VC. Atomization process for metal powder. *Mater Sci Eng A*. 2004;383(1):1-6.

doi: 10.1016/j.msea.2004.02.059

31. Strondl A, Lyckfeldt O, Brodin H, Ackelid U. Characterization and Control of Powder Properties for Additive Manufacturing. *JOM*. 2015;67(3):549-554.

doi: 10.1007/s11837-015-1304-0

32. Sutton AT, Kriewall CS, Leu MC, Newkirk JW. Powders for additive manufacturing processes: Characterization techniques and effects on prt properties. Reviewed paper presented at: Solid Freeform Fabrication 2016: Proceedings of the 26th Annual International Solid Freeform Fabrication Symposium – An Additive Manufacturing Conference; 2016. Austin, TX.

33. Slotwinski JA, Garboczi EJ, Stutzman PE, Ferraris CF, Watson SS, Peltz MA. Characterization of Metal Powders Used for Additive Manufacturing. *J Res Natl Inst Stand Technol*. 2014;119:460.

doi: 10.6028/jres.119.018

34. Baesso I, Karl D, Spitzer A, Gurlo A, Günster J, Zocca A. Characterization of powder flow behavior for additive manufacturing. *Addit Manuf*. 2021;47:102250.

doi: 10.1016/j.addma.2021.102250

35. Nguyen QB, Nai MLS, Zhu Z, Sun CN, Wei J, Zhou W. Characteristics of Inconel Powders for Powder-Bed Additive Manufacturing. *Engineering*. 2017;3(5):695-700.

doi: 10.1016/j.eng.2017.05.012

36. Yang Y, Gu D, Dai D, Ma C. Laser energy absorption behavior of powder particles using ray tracing method during selective laser melting additive manufacturing of aluminum alloy. *Mater Des*. 2018;143:12-19.

doi: 10.1016/j.matdes.2018.01.043

37. Nandwana P, Kirka MM, Paquit VC, Yoder S, Dehoff RR. Correlations Between Powder Feedstock Quality, In Situ

Porosity Detection, and Fatigue Behavior of Ti-6Al-4V Fabricated by Powder Bed Electron Beam Melting: A Step Towards Qualification. *JOM*. 2018;70(9):1686-1691.

doi: 10.1007/s11837-018-3034-6

38. Boyer RR. An overview on the use of titanium in the aerospace industry. *Mater Sci Eng A*. 1996;213(1-2):103-114.

doi: 10.1016/0921-5093(96)10233-1

39. Elias CN, Lima JHC, Valiev R, Meyers MA. Biomedical applications of titanium and its alloys. *JOM*. 2008;60(3):46-49.

doi: 10.1007/s11837-008-0031-1

40. Trevisan F, Calignano F, Aversa A, *et al.* Additive manufacturing of titanium alloys in the biomedical field: processes, properties and applications. *J App Biomat Func Mater* 2018;16(2):57-67.

doi: 10.5301/jabfm.5000371

41. Naqvi SMR, Gu J, Liu S, *et al.* Laser powder bed fusion additive manufacturing of Ti-6Al-4V dental implants with gradient porosity: Design, simulation, and biomechanical performance. *J Mater Sci*. 2025; 61(1):594–616.

doi: 10.1007/s10853-025-11880-9

42. Aufa AN, Hassan MZ, Ismail Z. Recent advances in Ti-6Al-4V additively manufactured by selective laser melting for biomedical implants: Prospect development. *J Alloys Compd*. 2022;896:163072.

doi: 10.1016/j.jallcom.2021.163072

43. Pasang T, Budiman AS, Wang JC, *et al.* Additive manufacturing of titanium alloys – Enabling re-manufacturing of aerospace and biomedical components. *Microelectron Eng*. 2023;270:111935.

doi: 10.1016/j.mee.2022.111935

44. García-Hernández C, García-Cabezón C, González-Diez F, *et al.* Effect of processing on microstructure, mechanical properties, corrosion and biocompatibility of additive manufacturing Ti-6Al-4V orthopaedic implants. *Sci Rep*. 2025;15(1).

doi: 10.1038/s41598-025-98349-6

45. Young Z, Qu M, Coday MM, *et al.* Effects of Particle Size Distribution with Efficient Packing on Powder Flowability and Selective Laser Melting Process. *Materials*. 2022;15(3):705.

doi: 10.3390/ma15030705

46. Haferkamp L, Haudenschild L, Spierings A, *et al.* The Influence of Particle Shape, Powder Flowability, and Powder Layer Density on Part Density in Laser Powder Bed Fusion. *Metals*. 2021;11(3):418.

doi: 10.3390/met11030418

47. Spurek MA, Haferkamp L, Weiss C, Spierings AB, Schleifenbaum JH, Wegener K. Influence of the particle size distribution of monomodal 316L powder on its flowability and processability in powder bed fusion. *Prog Addit Manuf*. 2022;7(4):533–542.

doi: 10.1007/s40964-021-00240-z

48. Chu F, Li E, Shen H, *et al.* Influence of powder size on defect generation in laser powder bed fusion of AlSi10Mg alloy. *J Manuf Process*. 2023;94:183-195.

doi: 10.1016/j.jmapro.2023.03.046

49. Dietrich K, Diller J, Dubiez-Le Goff S, Bauer D, Forêt P, Witt G. The influence of oxygen on the chemical composition and mechanical properties of Ti-6Al-4V during laser powder bed fusion (L-PBF). *Addit Manuf*. 2020;32:100980.

doi: 10.1016/j.addma.2019.100980

50. Dong YP, Li YL, Zhou SY, *et al.* Cost-affordable Ti-6Al-4V for additive manufacturing: Powder modification, compositional modulation and laser in-situ alloying. *Addit Manuf*. 2021;37:101699.

doi: 10.1016/j.addma.2020.101699

51. Wu Z, Asherloo M, Jiang R, *et al.* Study of printability and porosity formation in laser powder bed fusion built hydride-dehydride (HDH) Ti-6Al-4V. *Addit Manuf*. 2021;47:102323.

doi: 10.1016/j.addma.2021.102323

52. Soltani-Tehrani A, Habibnejad-Korayem M, Shao S, Haghshenas M, Shamsaei N. Ti-6Al-4V powder characteristics in laser powder bed fusion: The effect on tensile and fatigue behavior. *Addit Manuf*. 2022;51:102584.

doi: 10.1016/j.addma.2021.102584

53. Asherloo M, Wu Z, Delpazir MH, *et al.* Laser-beam powder bed fusion of cost-effective non-spherical hydride-dehydride Ti-6Al-4V alloy. *Addit Manuf*. 2022;56:102875-102875.

doi: 10.1016/j.addma.2022.102875

54. Meier B, Warchomicka F, Petrusa J, *et al.* Influence of powder production process and properties on material properties of Ti6Al4V manufactured by L-PBF. *Int J Adv Manuf Technol*. 2022;123(5-6):1577-1588.

doi: 10.1007/s00170-022-10250-y

55. Lu F, Ma Q, Liu E, *et al.* Advancements in understanding the microstructure and properties of additive manufacturing Ti-6Al-4V alloy: A comprehensive review. *J Alloys Comp*. 2025;1027:180543.

doi: 10.1016/j.jallcom.2025.180543

56. Asherloo M, Hwang J, Leroux R, *et al.* Understanding process-microstructure-property relationships in laser powder bed fusion of non-spherical Ti-6Al-4V powder. *Mater Charact*. 2023;198:112757-112757.

doi: 10.1016/j.matchar.2023.112757

57. Habibnejad-Korayem M, Lalh M, Schunk C, Zou Y.

Offsize particle size utilization for laser powder bed fusion processing of plasma atomized Ti-6Al-4V powders: Impacts on part properties and powder safety. *J Manuf Process*. 2023;107:559-573.

doi: 10.1016/j.jmapro.2023.10.036

58. Asherloo M, Ramadurai MS, Heim M, *et al.* Advancing laser powder bed fusion with non-spherical powder: Powder-process-structure-property relationships through experimental and analytical studies of fatigue performance. *Addit Manuf*. 2024;95:104534.

doi: 10.1016/j.addma.2024.104534

59. Kim M, Kim O, Song Y, *et al.* Cost-Effective Laser Powder Bed Fusion of Ti-6Al-4V Grade 5: The Effect of Expanding Powder Size Distribution on Mechanical Performance. *Materials*. 2024;18(1):6.

doi: 10.3390/ma18010006

60. Ludwig I, Kluge M. Investigation of an Increased Particle Size Distribution of Ti-6Al-4V Powders Used for Laser-Based Powder Bed Fusion of Metals. *Materials*. 2024;17(12):2942-2942.

doi: 10.3390/ma17122942

61. Gordon JV, Narra SP, Cunningham RW, *et al.* Defect structure process maps for laser powder bed fusion additive manufacturing. *Addit Manuf*. 2020;36:101552.

doi: 10.1016/j.addma.2020.101552

62. ASTM C1444-00. Standard Test Method for Measuring the Angle of Repose of Free-Flowing Mold Powders. West Conshohocken, PA, ASTM International, 2000.

63. ASTM B212-17. Standard Test Method for Apparent Density of Free-Flowing Metal Powders Using the Hall Flowmeter Funnel. West Conshohocken, PA, ASTM International, 2017.

doi: 10.1520/B0212-17

64. ASTM E8/E8M-16a, Standard Test Methods for Tension Testing of Metallic Materials, ASTM International, West Conshohocken, PA, 2016.

doi: 10.1520/E0008_E0008M-16A

65. Sun P, Fang ZZ, Zhang Y, Xia Y. Review of the Methods for Production of Spherical Ti and Ti Alloy Powder. *JOM*. 2017;69(10):1853-1860.

doi: 10.1007/s11837-017-2513-5

66. Boley CD, Khairallah SA, Rubenchik AM. Calculation of laser absorption by metal powders in additive manufacturing. *Appl Opt*. 2015;54(9):2477.

doi: 10.1364/ao.54.002477

67. Yin J, Wang D, Yang L, *et al.* Correlation between forming quality and spatter dynamics in laser powder bed fusion. *Addit Manuf*. 2020;31:100958.

doi: 10.1016/j.addma.2019.100958

68. Wang D, Wu S, Fu F, *et al.* Mechanisms and characteristics of spatter generation in SLM processing and its effect on the properties. *Mater Des*. 2017;117:121-130.

doi: 10.1016/j.matdes.2016.12.060

69. Lee Y, Simunovic S, A. Gurnon. Quantification of Powder Spreading Process for Metal Additive Manufacturing. *OSTI OAI US Dep Energy Off Sci Tech Inf.* Published online October 10, 2019.

doi: 10.2172/1615799

70. Anderson IE, White EMH, Dehoff R. Feedstock powder processing research needs for additive manufacturing development. *Curr Opin. Solid State Mater Sci*. 2018;22(1):8-15.

doi: 10.1016/j.cossms.2018.01.002

71. Seyda V, Kaufmann N, Emmelmann C. Investigation of Aging Processes of Ti-6Al-4 V Powder Material in Laser Melting. *Phys Procedia*. 2012;39:425-431.

doi: 10.1016/j.phpro.2012.10.057

72. Habibnejad-korayem M, Zhang J, Zou Y. Effect of particle size distribution on the flowability of plasma atomized Ti-6Al-4V powders. *Powder Technol*. 2021;392:536-543.

doi: 10.1016/j.powtec.2021.07.026

73. Abeyta A, Nouwens C, Jones AM, *et al.* Characterizing gas flow in the build chamber of laser powder bed fusion systems utilizing particle image velocimetry: A path to improvements. *Addit Manuf*. 2025;106:104810.

doi: 10.1016/j.addma.2025.104810

74. du Plessis A, Yadroitsev I, Yadroitsava I, Le Roux SG. X-Ray Microcomputed Tomography in Additive Manufacturing: A Review of the Current Technology and Applications. *3D Print Addit Manuf*. 2018;5(3):227-247.

doi: 10.1089/3dp.2018.0060

75. Poulin JR, Kreitcberg A, Brailovski V. Effect of hot isostatic pressing of laser powder bed fused Inconel 625 with purposely induced defects on the residual porosity and fatigue crack propagation behavior. *Addit Manuf*. 2021;47:102324.

doi: 10.1016/j.addma.2021.102324

76. Gao H, Zhang Z, Li J, *et al.* Hot isostatic pressing elimination of process-induced defects in laser powder bed fusion fabricated DZ125 superalloy: Microstructure evolution and mechanical property enhancement. *J Mater Res Technol*. 2025;37:3907-3923.

doi: 10.1016/j.jmrt.2025.07.069

77. Mahtabi M, Yadollahi A, Ataollahi S, Mahtabi MJ. Effect of build height on structural integrity of Ti-6Al-4V fabricated via laser powder bed fusion. *Eng Fail Anal*. 2023;154:107691.

doi: 10.1016/j.engfailanal.2023.107691

78. Xue M, Chen X, Ji X, Xie X, Chao Q, Fan G. Effect of Particle Size Distribution on the Printing Quality and Tensile Properties of Ti-6Al-4V Alloy Produced by LPBF Process. *Metals*. 2023;13(3):604-604.

doi: 10.3390/met13030604

79. Brika SE, Letenneur M, Dion CA, Brailovski V. Influence of particle morphology and size distribution on the powder flowability and laser powder bed fusion manufacturability of Ti-6Al-4V alloy. *Addit Manuf*. 2020;31:100929.

doi: 10.1016/j.addma.2019.100929

Appendix

Calculating mass of powder and age of powder for each build

The given data is as follows:

Build	Mass in build (kg)	Mass after build (kg)
Build 1	30	25.8
Build 2	30	29.2
Build 3	30	28.4
Build 4	30	28.5
Build 5	30	28.4
Build 6	29.1	26.0

The following table was constructed using the methods described below:

Powder Age	Build 1	Build 2	Build 3	Build 4	Build 5	Build 6
Virgin (kg)	30	4.2	0.8	1.6	1.5	0.7
1 Build (kg)	0	25.8	4.1	0.7	1.5	1.4
2 Builds (kg)	0	0	25.1	3.9	0.7	1.4
3 Build (kg)	0	0	0	23.7	3.7	0.7
4 Build (kg)	0	0	0	0	22.5	3.5
5 Build (kg)	0	0	0	0	0	21.3

Let $m_{x,i}$ be the mass in build for build x and let $m_{x,o}$ be the mass after build for build x. The virgin powder added for the next build is as follows

$$V_{x+1} = m_{x,i+1} - m_{x,o}$$

where V_x describes the mass of virgin powder added for build x. For example, the virgin powder added in Build 5 is as follows:

$$V_5 = m_{5,i} - m_{4,o}$$

The assumption for powder use was that an equal fraction of powder from each age group was used in the creation of the final products. Let $m_{x.y}$ be the mass in build x that has been reused y times.

$$m_{x,y} = \frac{m_{x-1,y-1}}{m_{x,i}} \cdot m_{x-1,o}$$

For example, the mass of powder in build 5 that has a powder age of 3 build cycles is as follows:

$$m_{5,3} = \frac{m_{4,2}}{m_{5,i}} \cdot m_{4,o}$$

Using this nomenclature, the virgin powder added can also be described as follows:

$$V_x = m_{x,0}$$

As a sanity check, each build should total the mass in build $m_{x,o}$.

$$m_{x,o} = \sum_0^n m_{x,n}$$

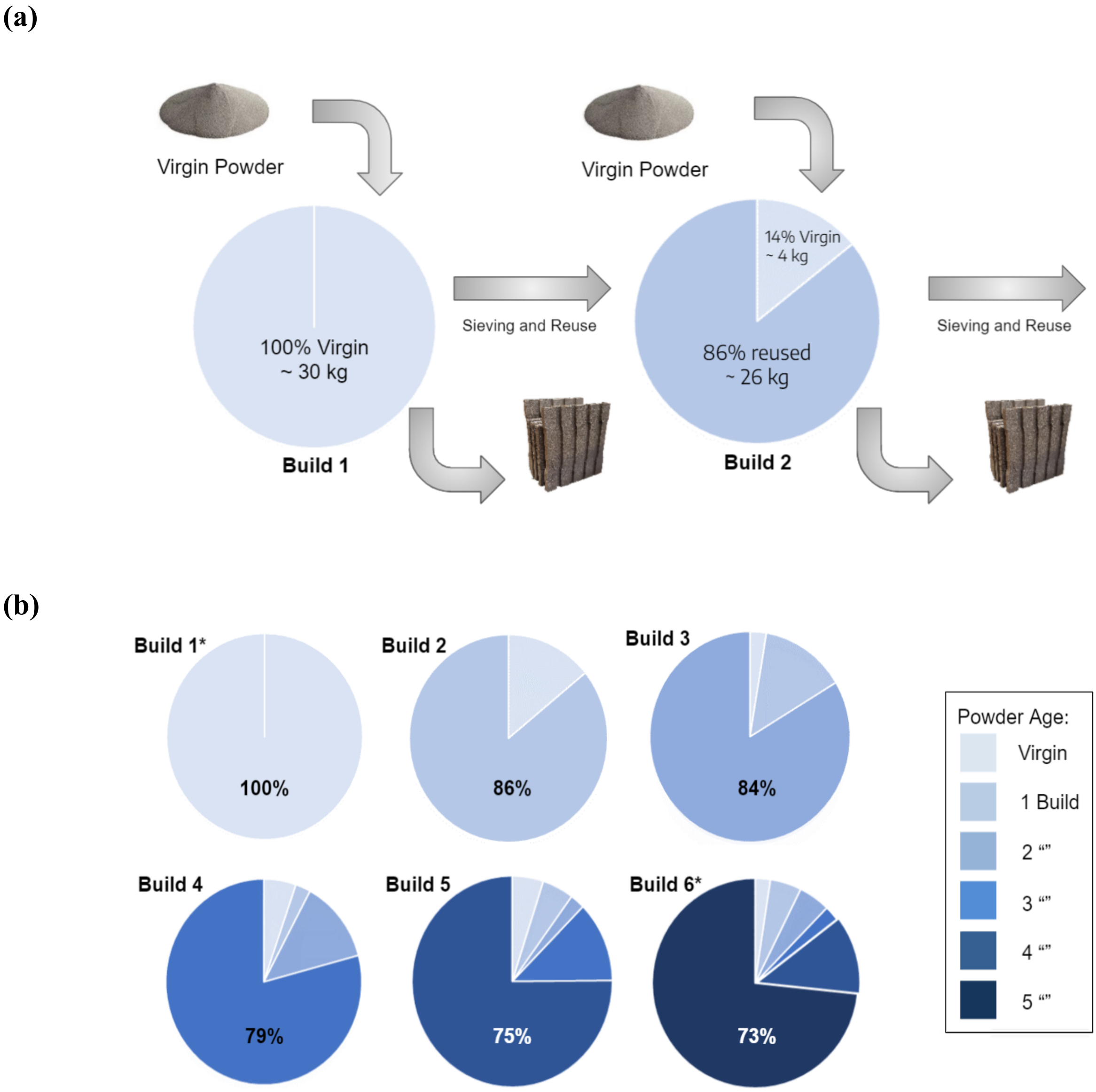

Figure A1. Powder reuse schedule. (a) Schematic description of the powder reuse process. (b) Percentages of reused and virgin powder for each build.

Table A1. Powder composition by mass (in kg) of each build

Powder age	Build 1	Build 2	Build 3	Build 4	Build 5	Build 6
Virgin (kg)	30	4.2	0.8	1.6	1.5	0.7
1 Build (kg)	0	25.8	4.1	0.7	1.5	1.4
2 Build (kg)	0	0	25.1	3.9	0.7	1.4
3 Build (kg)	0	0	0	23.7	3.7	0.7
4 Build (kg)	0	0	0	0	22.5	3.5
5 Build (kg)	0	0	0	0	0	21.3

Table A2. Inert gas fusion tests for PA and GA samples after first, third and sixth build

Powder IGF Sample	Oxygen(wt.%)	Nitrogen(wt.%)	Hydrogen(wt. %)
PA Build 1	0.163	0.0156	0.0027
PA Build 3	0.169	0.0163	0.0027
PA Build 6	0.167	0.0153	0.0027
GA Build 1	0.123	0.0100	0.0015
GA Build 3	0.136	0.0135	0.0015
GA Build 6	0.135	0.0124	0.0019

Table A3. Summary of powder parameters of the PA powder in the reuse process

Parameters	Virgin	Build 1	Build 2	Build 3	Build 4	Build 5	Build 6
Hall flow (s)	N/A	27.7	N/A	28.5	N/A	N/A	28.2
Apparent density (g/cm^3)	2.59	2.63	N/A	2.62	N/A	N/A	2.61
D10	30	28.2	28	28.1	28.1	27.8	28.8
D50	41	37.9	38.3	38.5	38.7	38.4	40.1
D90	57	52.6	54.3	54.7	55.5	55	57.9

Table A4. Summary of powder parameters of the GA powder in the reuse process

Parameters	Virgin	Build 1	Build 2	Build 3	Build 4	Build 5	Build 6
Angle of Repose(degree)	36	35	36	33	37	31	28
Apparent Density(g/cm3)	2.34	2.38	2.45	2.31	2.27	2.32	2.29
D10(μm)	17.5	16.0	16.5	16.1	18.2 17.7	16.8	
D50(μm)	26.8	26.9	26.8	27.2	28.4	28.3	27.3
D90(μm)	40.6	45.5	41.8	44.4	43.1	44.4	42.5